PHYSICAL REVIEW C **86**, 034326 (2012)

Possible antimagnetic rotational band and neutron alignment in ^{101}Pd

M. Sugawara*
Chiba Institute of Technology, Narashino, Chiba 275-0023, Japan

T. Hayakawa, M. Oshima, Y. Toh, A. Osa, M. Matsuda, T. Shizuma, and Y. Hatsukawa
Japan Atomic Energy Agency, Tokai, Ibaraki 319-1195, Japan

H. Kusakari
Chiba University, Inage-ku, Chiba 263-8522, Japan

T. Morikawa
Kyushu University, Hakozaki, Fukuoka 812-8581, Japan

Z. G. Gan
Institute of Modern Physics, Chinese Academy of Science, Lanzhou 730000, P.R. China

T. Czosnyka
Heavy Ion Laboratory, Warsaw PL-02097, Poland

(Received 9 May 2012; revised manuscript received 23 July 2012; published 18 September 2012)

High-spin states of ^{101}Pd were studied through in-beam γ-ray spectroscopy by using the reaction ^{68}Zn(^{37}Cl, $1p3n$). The band based on the $h_{11/2}$ neutron orbital was extended up to $(\frac{51}{2}^{-})$, and the band based on the $d_{5/2}$ neutron orbital was revised. Various transitions decaying to these bands were observed, and consequently several side bands were established. Electric dipole transitions from the $\nu h_{11/2}$ band to the $\nu d_{5/2}$ band were also observed. The structure of the $\nu h_{11/2}$ band is discussed from the viewpoint of antimagnetic rotation based on a semiclassical particle-rotor model by taking neutron alignments into account. The possible existence of octupole correlations is also discussed on the basis of $B(E1)/B(E2)$ ratios for the decays of the $\nu h_{11/2}$ band.

DOI: 10.1103/PhysRevC.86.034326 PACS number(s): 23.20.−g, 21.10.Re, 25.70.−z, 27.60.+j

I. INTRODUCTION

Research in the last two decades has revealed that particle-hole combinations of dissimilar nucleons occupying high-j orbitals can produce novel structures known as magnetic rotation (MR) bands and antimagnetic rotation (AMR) bands [1,2] around doubly magic nuclei. What is novel is that these bands show a regular rotational behavior despite the small deformation of the nuclei. This phenomenon is explained by what is now known as the shears mechanism, in which the total angular momentum is generated by gradually aligning the constituent angular momenta of high-j orbitals to one another. The MR band can be easily distinguished from the normal rotational band in that it consists almost exclusively of $M1$ cascade transitions, while $E2$ crossover transitions are weak, if observed at all. In this respect, the AMR band is subtle as it consists of stretched $E2$ transitions, which is similar to the normal rotational band. Lifetime measurements are necessary to show the decrease in $B(E2)$ values with respect to the increasing spin and to confirm that the total angular momentum is generated by the shears mechanism. Consequently, evidence of AMR has been reported in only a few cases thus far, and therefore searching for new possible AMR bands is still beneficial in terms of selecting candidates for future lifetime measurements.

It is important to note at this point that there is another interesting phenomenon known as band termination, which is related to the alignment of angular momenta of valence nucleons. In fact, it was pointed out by Simons *et al.* [3] that the band properties might change gradually from AMR near closed shells to the collective rotation of well-deformed nuclei in the middle of a shell. Therefore, rotational bands, including high-j particle-hole configurations of dissimilar nucleons, can be expected to exhibit the characteristics of AMR when approaching band termination.

The phenomenon of band termination has been commonly observed in neutron-deficient nuclei below the Sn isotope chain, close to the doubly magic ^{100}Sn. For example, multiple band terminations have been found in ^{100}Pd [4], ^{102}Pd [5], and ^{101}Ag [6]. Relevant high-j orbitals for AMR in this region are $\pi g_{9/2}$ as a hole state and $\nu h_{11/2}$, $\nu g_{7/2}$, and $\nu d_{5/2}$ as particle states. In this regard, AMR bands have been confirmed in ^{105}Cd [7], ^{106}Cd [3], and ^{108}Cd [8,9], as well as tentatively in ^{100}Pd [10], ^{109}Cd [11], and ^{110}Cd [2]. In this article, we report the results of an in-beam γ-ray study on high-spin states of ^{101}Pd and discuss the possibility that the $\nu h_{11/2}$ band may be of AMR character before band termination.

---

[*] masahiko.sugawara@it-chiba.ac.jp

Prior to this work, there have been several γ-ray spectroscopic studies on ^{101}Pd, whereby detailed knowledge of low-spin states has been obtained by studying the decay of ^{101}Ag [12,13]. High-spin states have been investigated via ^{12}C-induced reactions, and two bands based on $\nu d_{5/2}$ and $\nu h_{11/2}$ orbitals have been observed [14,15]. These bands have been extended recently in a study using the ^{76}Ge(^{28}Si, $3n\gamma$) reaction [16,17].

This paper is organized as follows. First, we describe the experimental methods and results in Sec. II. The discussion in Sec. III includes the description of the $\nu h_{11/2}$ band on the basis of the semiclassical particle-rotor model with neutron alignments, and the results of model calculations are compared with experimental data in the same section. Lastly, a summary is given in Sec. IV.

II. EXPERIMENTAL METHODS AND RESULTS

In-beam γ-ray spectroscopy was performed on ^{101}Pd through the reaction ^{68}Zn(^{37}Cl, $1p3n$). An enriched ^{68}Zn foil with a thickness of 9 mg/cm^2 was bombarded with a 125 MeV ^{37}Cl beam provided by the tandem accelerator at the Japan Atomic Energy Agency (JAEA), whereby γ rays emitted from the excited states were detected with an array of 12 HPGe detectors with BGO Compton suppressors (GEMINI) [18]. The HPGe detectors were placed at angles of 32°, 58°, 90°, 122°, and 148° with respect to the beam direction. The energy resolution of the HPGe detectors was 1.8–2.7 keV at 1.3 MeV, and the experimental data were recorded on magnetic tapes on an event-by-event basis when two or more detectors were fired. A total of 2.9×10^8 events were collected during three days of beam time. Multiple γ-γ coincidence events were sorted into $E_\gamma - E_\gamma$ matrices, and the level scheme was constructed from these matrices using software written by Radford [19]. The relative intensities of γ rays were obtained from the gated spectra. For the level spin assignments, we used the γ-ray coincidence intensity ratios $I(\gamma_1{:}32^\circ \text{ or } 148^\circ, \gamma_2{:}\text{all})/I(\gamma_1{:}90^\circ, \gamma_2{:}\text{all})$, and $I(\gamma_1{:}58^\circ \text{ or } 122^\circ, \gamma_2{:}\text{all})/I(\gamma_1{:}90^\circ, \gamma_2{:}\text{all})$ (angular distribution from oriented nuclei (ADO) ratios) [20]. Here, $I(\gamma_1{:}\theta, \gamma_2{:}\text{all})$ corresponds to the γ-ray coincidence intensity observed by the detectors at an angle θ by setting gates on the detectors at any angle. To obtain these ratios, we sorted γ-γ coincidence events to three asymmetric matrices whose x axes were the γ-ray energies in the detector at 32° or 148°, 58° or 122°, and 90°, while the y axes for these matrices were the γ-ray energies in the detector at any position. Although several transitions exhibit multiplet structures, ADO ratios were obtained separately for individual components whenever it was possible to set the proper gate. Typical ADO (32°/90°) ratios observed for the known γ rays in this experiment were 1.3 for stretched quadrupole transitions and 0.7 for stretched pure dipole transitions. Therefore, we assigned the stretched quadrupole transition (stretched dipole transition) to ratios around 1.3 (around 0.7) for the new γ rays.

The total projection spectrum of the $E_\gamma - E_\gamma$ matrix, which is shown in Fig. 1, indicates that ^{101}Pd was a major product of the present reaction. Examples of γ-γ coincidence spectra are presented in Figs. 2 and 3 as an illustration of the band structure in the proposed level scheme. The spectrum obtained by setting a gate on the 678-keV transition from $\frac{11}{2}^+$ to $\frac{7}{2}^+$ is shown in Fig. 2(a), which suggests the existence of a 1104-keV transition within the band. Furthermore, the spectrum in Fig. 2(b), obtained by setting a gate on the 748-keV transition from $\frac{19}{2}^-$ to $\frac{15}{2}^-$, includes a cascade of 936-, 1045-, 987-, and 1097-keV transitions. Moreover, the spectrum in Fig. 2(c), obtained by setting a gate on the 667-keV transition from $\frac{9}{2}^+$ to $\frac{5}{2}^+$, clearly confirms the existence of a 1204-keV transition within the band. Since a thick target was used in the present experiment, we assumed that γ rays emitted from higher-lying states would suffer from the Doppler broadening effect due to slowing-down processes. Therefore, the γ-ray spectra obtained by projecting one of the three asymmetric matrices onto the x axis (90°) are shown in Fig. 3, where rather broad peaks at 1423, 1033, and 1494 keV appear in both spectra obtained by setting gates on the cascade of 971 and 911 keV in the known negative-parity band, where the broadening at 1423 keV appears to be wider than that at 1033 keV. To clarify this point, part of the spectrum obtained by projecting one of the three asymmetric matrices onto the x axis ($\theta = 58^\circ, 122^\circ$) is provided as an inset in Fig. 3(a). The inset shows that the shifts for forward and backward angles at the 1033- and 1423-keV lines are rather similar. Since the 1494-keV line is too weak to be recognized in Fig. 3(b), a vertically expanded spectrum for the high-energy region around 1423 keV is provided as an inset showing that the broadening for the 1494-keV peak is similar to that for the 1423-keV peak. Due to the weakness of these three transitions, we cannot show that they are in mutual coincidence, and therefore, the possibility that they occur in parallel can not be ruled out. However, if the 1033-keV transition were a side-feeder to band 3, it would have been observed in the experiment conducted by Zhou *et al.* using the ^{76}Ge(^{28}Si, $3n\gamma$) reaction [16,17]. Taking into account the fact that our reaction should be more efficient in populating high-spin states, we placed the

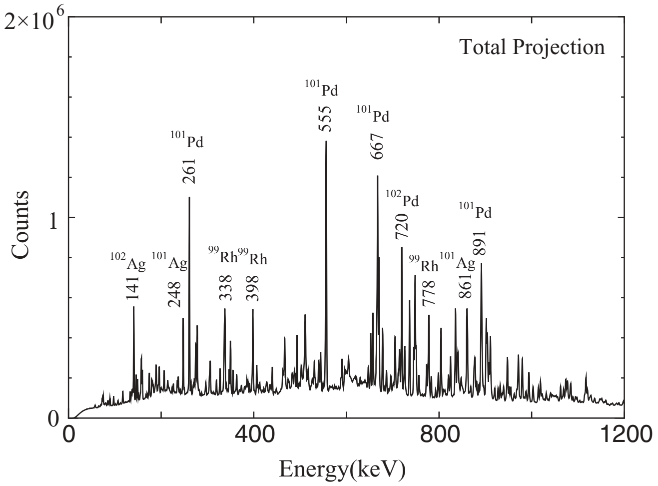

FIG. 1. Total projection spectrum of the $E_\gamma - E_\gamma$ matrix. Only prominent transitions of main reaction products are marked with their energies and nuclide symbols.

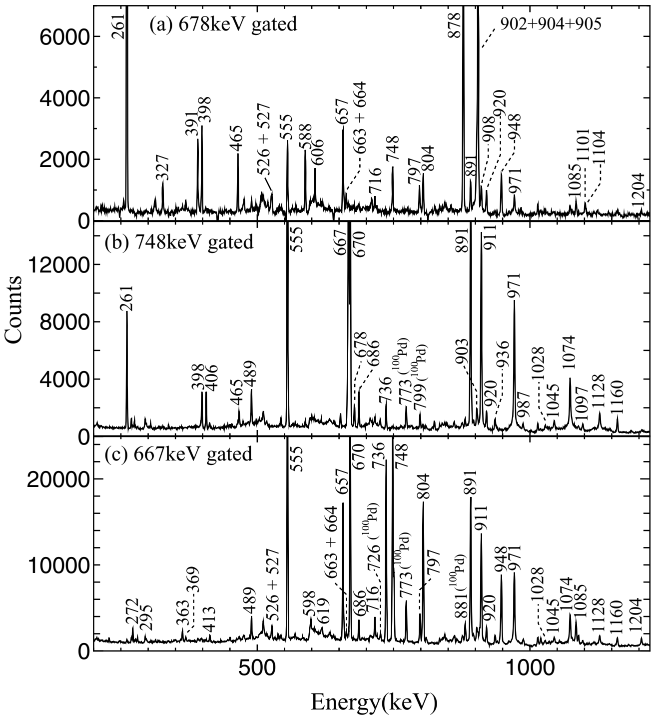

FIG. 2. Examples of γ-γ coincidence spectra obtained by setting gates on the lower-lying transitions of known bands. These spectra were obtained from the $E_\gamma - E_\gamma$ matrix and provide confirmation for the results of previous experiments. Energy values are given above the peaks in units of keV. (a) A spectrum obtained by setting a gate on the 678-keV transition from $\frac{11}{2}^{+}$ to $\frac{7}{2}^{+}$, which includes one in band 2 and another in band 6. (b) A spectrum obtained by setting a gate on the 748-keV transition from $\frac{19}{2}^{-}$ to $\frac{15}{2}^{-}$. (c) A spectrum obtained by setting a gate on the 667-keV transition from $\frac{9}{2}^{+}$ to $\frac{5}{2}^{+}$.

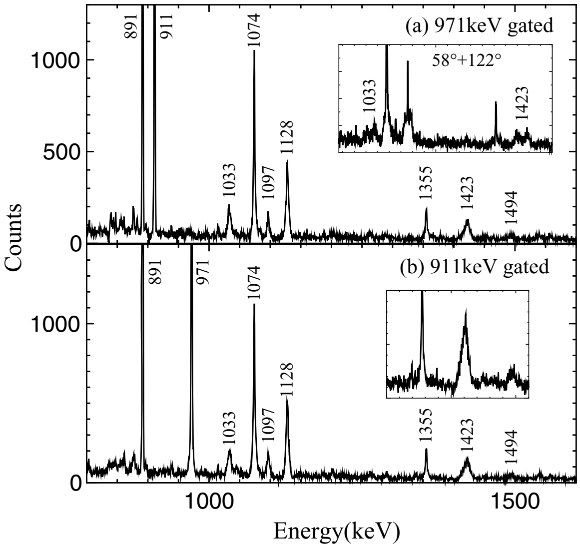

FIG. 3. Examples of γ-γ coincidence spectra obtained by setting gates on the higher-lying transitions of the known negative-parity band. These spectra, which were obtained by projecting one of the three asymmetric matrices onto the x axis (90°) to avoid broadening due to the Doppler shifts at other angles, can be used to extend the band to higher-spin states. Energy values are given above the peaks in units of keV. (a) A spectrum obtained by setting a gate on the 971-keV transition from $\frac{31}{2}^{-}$ to $\frac{27}{2}^{-}$. The inset shows part of the spectrum obtained by projecting one of the three asymmetric matrices onto the x axis ($\theta = 58°$, 122°). (b) A spectrum obtained by setting a gate on the 911-keV transition from $\frac{27}{2}^{-}$ to $\frac{23}{2}^{-}$. The inset shows a vertically expanded spectrum for the high-energy region around 1423 keV.

1033- and 1494-keV transitions in a cascade above $\frac{43}{2}^{-}$, in accordance with the order determined from the intensity relation. We also extracted the ADO ratios and assigned quadrupoles to both the 1423- and 1033-keV transitions owing to the clean spectra obtained by setting appropriate gates.

The properties of the γ rays observed in this experiment are summarized in Table I, and the level scheme for ^{101}Pd established in this experiment is shown in Fig. 4, where the observed bands are labeled 1 to 6. Bands 1, 2, 3, and 6 were observed by Popli *et al.* [15] to $\frac{29}{2}^{+}$, $\frac{23}{2}^{+}$, one state above $(\frac{31}{2}^{-})$ with no spin assignment, and $\frac{15}{2}^{+}$, respectively. Recently, bands 1 and 3 were extended to $(\frac{33}{2}^{+})$ and $(\frac{43}{2}^{-})$, respectively, in an experiment conducted by Zhou *et al.* [16,17], who also observed band 4 (labeled as "structure 2" in Ref. [16]) and the high-spin part of band 2 ($\geqslant \frac{27}{2}^{+}$:labeled as "structure 1" in Ref. [16]).

In the present experiment, we extended bands 3 and 6 to higher spins by $4\hbar$ and $2\hbar$, respectively. Band 5 is a new band which was found to decay to bands 3 and 4. The low-spin part of band 2 was observed up to $\frac{23}{2}^{+}$ by Zhou *et al.* (labeled as "band 2" in Ref. [16]). An expanded plot of the spectrum obtained by setting gates on the 904- and 905-keV transitions in band 2 is shown Fig. 5, in which a 902-keV peak is clearly seen as a shoulder. We observed the 902-keV transition between $\frac{27}{2}^{+}$ and $\frac{23}{2}^{+}$. In this way, "structure 1" and "band 2" are in fact merged into band 2 presented here. Figure 6 shows a γ-γ coincidence spectrum obtained by setting a gate on the 716-keV transition from $\frac{27}{2}^{+}$ in band 2 to $\frac{25}{2}^{+}$ in band 1. The 1189-keV transition, which was claimed to be between $\frac{31}{2}^{+}$ and $\frac{27}{2}^{+}$ by Zhou *et al.* [16], was not observed, as shown in Fig. 6(b). Instead, the spectrum in Fig. 6(a) suggests that the 1189-keV transition should be replaced by a cascade of 526- and 663-keV transitions. In addition to this refinement of band 2, several transitions to or from band 1 were newly observed. The properties of these transitions, including known ones, are summarized in terms of $B(M1)/B(E2)$ ratios in Table II, where dipole and quadrupole transitions are assumed to be pure $M1$ and pure $E2$ transitions, respectively. The table also shows the upper and lower bounds derived by taking $I_\gamma = 0.1$ in cases where either $M1$ or $E2$ has not been observed. Several $E1$ transitions from band 3 to band 1 were observed in the low-spin region in this experiment. The properties of these transitions are summarized in terms of $B(E1)/B(E2)$ ratios in Table III where similar $E1$ transitions in ^{100}Pd are also tabulated for comparison. Band 5 decays to band 3 via $E2$ transitions and to band 4 via $M1$ transitions, and the properties of these transitions are summarized in terms of $B(E2)$ ratios and $B(M1)/B(E2)$ ratios in Table IV.

TABLE I. Properties of γ rays observed in this experiment. Relative intensities are normalized to that of the 667-keV transition from $\frac{9}{2}^+$ to $\frac{5}{2}^+$. ADO ratios are tabulated for different combinations of detectors.

$I_\mathrm{i} \rightarrow I_\mathrm{f}$	E_γ(keV)	I_γ	ADO (32°/90°)	ADO (58°/90°)	Multipolarity
$\frac{3}{2}^+ \rightarrow \frac{5}{2}^+$	80.2(1)	2(1)			
$(\frac{17}{2}^-) \rightarrow \frac{19}{2}^-$	141.0(1)	0.47(7)			
$\frac{21}{2}^+ \rightarrow \frac{19}{2}^+$	143.5(1)	0.17(1)			
$\frac{17}{2}^+ \rightarrow \frac{15}{2}^+$	144.5(2)	0.20(4)			
$\frac{19}{2}^+ \rightarrow \frac{21}{2}^+$	169.5(1)	0.36(2)	0.54(8)	1.0(1)	Dipole
$\frac{7}{2}^+ \rightarrow \frac{3}{2}^+$	180.6(1)	0.09(2)			
$\frac{7}{2}^+ \rightarrow \frac{5}{2}^+$	261.0(1)	40(20)			
$\frac{23}{2}^- \rightarrow \frac{23}{2}^-$	269.2(1)	0.46(3)	1.1(2)	1.4(2)	$\Delta I = 0$ dipole
$\frac{11}{2}^+ \rightarrow \frac{9}{2}^+$	271.8(1)	1.48(9)	0.70(6)	0.94(7)	Dipole
$\frac{35}{2}^- \rightarrow \frac{35}{2}^-$	281.1(1)	0.1(1)			$\Delta I = 0$ dipole
$\frac{17}{2}^- \rightarrow \frac{15}{2}^-$	287.3(2)	0.05(5)			
$\frac{27}{2}^- \rightarrow \frac{27}{2}^-$	294.6(1)	0.53(3)	1.3(2)	1.3(2)	$\Delta I = 0$ dipole
$\frac{7}{2}^+ \rightarrow \frac{7}{2}^+$	326.9(1)	2.1(1)	1.06(5)	1.04(5)	$\Delta I = 0$ dipole
$\frac{21}{2}^+ \rightarrow \frac{21}{2}^+$	362.7(1)	1.21(7)	0.73(7)	0.84(8)	$\Delta I = 0$ quadrupole
$\frac{29}{2}^+ \rightarrow \frac{27}{2}^+$	369.0(1)	1.08(7)	0.41(7)	0.8(1)	Dipole
$\frac{17}{2}^+ \rightarrow \frac{15}{2}^+$	390.9(1)	2.8(2)	0.58(3)	0.85(4)	Dipole
$\frac{11}{2}^- \rightarrow \frac{11}{2}^+$	398.5(1)	3.7(2)	1.12(5)	1.10(5)	$\Delta I = 0$ dipole
$\frac{9}{2}^+ \rightarrow \frac{7}{2}^+$	406.3(1)	6.7(3)	0.87(3)	0.89(3)	Dipole
$\frac{15}{2}^+ \rightarrow \frac{13}{2}^+$	413.2(1)	0.79(5)	0.58(8)	0.8(1)	Dipole
$\frac{19}{2}^- \rightarrow \frac{17}{2}^+$	433.5(2)	0.3(1)	0.6(2)	0.8(2)	Dipole
$\frac{25}{2}^- \rightarrow \frac{23}{2}^-$	446.2(1)	0.25(2)	0.6(2)	0.7(2)	Dipole
$\frac{13}{2}^+ \rightarrow \frac{11}{2}^+$	464.5(1)	2.6(1)	0.56(3)	0.88(5)	Dipole
$\frac{23}{2}^- \rightarrow \frac{21}{2}^-$	474.1(1)	0.79(4)	0.4(1)	0.8(2)	Dipole
$\frac{15}{2}^- \rightarrow \frac{13}{2}^+$	489.5(1)	3.9(2)	0.61(3)	0.79(4)	Dipole
$\frac{27}{2}^- \rightarrow \frac{25}{2}^-$	489.9(2)	0.33(3)	0.56(6)	0.60(7)	Dipole
$\frac{7}{2}^+ \rightarrow \frac{3}{2}^+$	508.0(1)	1.3(1)			
$\frac{19}{2}^+ \rightarrow \frac{17}{2}^+$	513.7(1)	1.44(9)	0.7(2)	1.0(2)	Dipole
$\frac{31}{2}^- \rightarrow \frac{29}{2}^+$	518.6(1)	0.56(3)	0.6(1)	0.9(1)	Dipole
$\frac{31}{2}^+ \rightarrow \frac{29}{2}^+$	525.7(1)	1.35(7)	0.50(6)	0.71(8)	Dipole
$\frac{21}{2}^- \rightarrow \frac{17}{2}^-$	527.0(1)	2.9(2)	1.2(1)	1.2(1)	Quadrupole
$\frac{7}{2}^+ \rightarrow \frac{3}{2}^+$	543.5(1)	0.32(3)			
$\frac{15}{2}^- \rightarrow \frac{11}{2}^-$	555.5(1)	62(3)	1.33(4)	1.22(4)	Quadrupole
$\frac{7}{2}^+ \rightarrow \frac{5}{2}^+$	588.1(2)	13(1)			
$\frac{11}{2}^+ \rightarrow \frac{9}{2}^+$	598.3(1)	4.8(4)	0.31(6)	0.66(8)	Dipole
$\frac{21}{2}^- \rightarrow \frac{19}{2}^+$	606.0(1)	2.3(1)	0.56(5)	0.81(6)	Dipole
$\frac{15}{2}^- \rightarrow \frac{15}{2}^-$	618.7(1)	2.8(2)	1.29(9)	1.19(9)	$\Delta I = 0$ dipole
$\frac{27}{2}^- \rightarrow \frac{25}{2}^+$	631.0(2)	0.26(3)			
$\frac{31}{2}^- \rightarrow \frac{29}{2}^-$	632.2(1)	0.77(5)			
$\frac{27}{2}^- \rightarrow \frac{23}{2}^-$	641.3(1)	0.28(3)			
$\frac{21}{2}^+ \rightarrow \frac{17}{2}^+$	657.3(1)	36(2)	1.39(5)	1.21(4)	Quadrupole
$\frac{29}{2}^+ \rightarrow \frac{27}{2}^+$	663.4(1)	2.5(2)	0.46(6)	0.64(7)	Dipole
$\frac{23}{2}^- \rightarrow \frac{21}{2}^+$	663.6(1)	0.26(6)			
$\frac{9}{2}^+ \rightarrow \frac{5}{2}^+$	667.5(1)	100(5)			
$\frac{11}{2}^- \rightarrow \frac{9}{2}^+$	670.4(1)	59(3)	0.62(2)	0.85(3)	Dipole
$\frac{11}{2}^+ \rightarrow \frac{7}{2}^+$	677.8(1)	4.6(3)	1.29(6)	1.17(6)	Quadrupole
$\frac{31}{2}^- \rightarrow \frac{27}{2}^-$	678.1(1)	0.22(4)			

TABLE I. *(Continued.)*

$I_i \rightarrow I_f$	E_γ (keV)	I_γ	ADO (32°/90°)	ADO (58°/90°)	Multipolarity
$\frac{11}{2}^+ \rightarrow \frac{7}{2}^+$	678.2(1)	29(2)	1.42(4)	1.14(4)	Quadrupole
$\frac{21}{2}^- \rightarrow \frac{19}{2}^-$	686.3(1)	5.3(3)	1.25(6)	1.10(6)	Mixed
$\frac{27}{2}^+ \rightarrow \frac{25}{2}^+$	715.8(1)	6.3(3)	0.70(4)	0.91(5)	Dipole
$\frac{35}{2}^+ \rightarrow \frac{33}{2}^+$	719.5(1)	2.5(2)	0.89(4)	0.91(5)	Dipole
$\frac{13}{2}^+ \rightarrow \frac{9}{2}^+$	736.4(1)	45(2)	1.31(4)	1.23(4)	Quadrupole
$\frac{19}{2}^- \rightarrow \frac{15}{2}^-$	748.4(1)	58(3)	1.40(4)	1.25(4)	Quadrupole
$\frac{15}{2}^+ \rightarrow \frac{11}{2}^+$	797.4(1)	3.2(2)	1.32(8)	1.10(8)	Quadrupole
$\frac{17}{2}^+ \rightarrow \frac{13}{2}^+$	804.3(1)	39(2)	1.34(4)	1.19(4)	Quadrupole
$\frac{31}{2}^+ \rightarrow \frac{29}{2}^+$	820.0(1)	0.43(3)	0.68(8)	0.8(1)	Dipole
$\frac{15}{2}^+ \rightarrow \frac{11}{2}^+$	877.9(1)	22(1)	1.36(4)	1.10(4)	Quadrupole
$\frac{17}{2}^+ \rightarrow \frac{13}{2}^+$	886.6(1)	1.3(1)	1.27(6)	1.12(5)	Quadrupole
$\frac{23}{2}^- \rightarrow \frac{19}{2}^-$	891.3(1)	47(2)	1.32(6)	1.15(6)	Quadrupole
$\frac{19}{2}^+ \rightarrow \frac{15}{2}^+$	891.6(2)	1.6(2)	1.35(8)	1.18(7)	Quadrupole
$\frac{27}{2}^+ \rightarrow \frac{23}{2}^+$	901.9(1)	4.5(2)	1.3(1)	1.06(9)	Quadrupole[a]
$\frac{29}{2}^- \rightarrow \frac{25}{2}^-$	902.5(1)	6.6(4)	1.22(7)	1.07(6)	Quadrupole
$\frac{23}{2}^+ \rightarrow \frac{19}{2}^+$	904.5(1)	11.1(6)	1.4(1)	1.1(1)	Quadrupole
$\frac{19}{2}^+ \rightarrow \frac{15}{2}^+$	904.9(1)	13.8(7)	1.34(4)	1.03(3)	Quadrupole[b]
$\frac{17}{2}^- \rightarrow \frac{15}{2}^-$	907.7(1)	5.0(3)	0.93(8)	0.99(8)	Dipole
$\frac{27}{2}^- \rightarrow \frac{23}{2}^-$	910.8(1)	36(2)	1.24(4)	1.15(4)	Quadrupole
$\frac{25}{2}^- \rightarrow \frac{21}{2}^-$	920.4(1)	6.7(3)	1.25(8)	1.02(7)	Quadrupole
$\frac{27}{2}^- \rightarrow \frac{23}{2}^-$	936.2(1)	2.6(1)	1.3(1)	1.1(1)	Quadrupole
$\frac{21}{2}^+ \rightarrow \frac{17}{2}^+$	936.3(1)	0.58(5)	1.3(2)	0.9(2)	Quadrupole
$\frac{25}{2}^+ \rightarrow \frac{21}{2}^+$	947.7(1)	26(1)	1.28(4)	1.18(4)	Quadrupole
$\frac{31}{2}^- \rightarrow \frac{27}{2}^-$	971.4(1)	26(1)	1.11(4)	1.06(4)	Quadrupole
$\frac{17}{2}^- \rightarrow \frac{15}{2}^+$	983.8(1)	0.74(5)	0.5(1)	0.8(2)	Dipole
$\frac{35}{2}^- \rightarrow \frac{31}{2}^-$	987.4(1)	1.39(8)	1.07(8)	0.91(8)	Quadrupole
$\frac{21}{2}^+ \rightarrow \frac{17}{2}^+$	1019.9(1)	2.2(1)	1.4(1)	1.1(1)	Quadrupole
$\frac{33}{2}^- \rightarrow \frac{29}{2}^-$	1028.0(1)	1.65(9)	1.3(3)	1.1(3)	Quadrupole
$\frac{47}{2}^- \rightarrow \frac{43}{2}^-$	1032.6(1)	0.52(5)	1.47(8)	1.40(8)	Quadrupole
$\frac{31}{2}^- \rightarrow \frac{27}{2}^-$	1044.6(1)	2.5(1)	1.2(1)	1.1(1)	Quadrupole
$\frac{35}{2}^- \rightarrow \frac{31}{2}^-$	1073.8(1)	12.8(7)	1.11(5)	1.03(5)	Quadrupole
$\frac{29}{2}^+ \rightarrow \frac{25}{2}^+$	1084.6(1)	9.0(5)	1.21(5)	1.18(5)	Quadrupole
$\frac{39}{2}^- \rightarrow \frac{35}{2}^-$	1096.9(1)	1.55(8)	1.3(2)	1.1(2)	Quadrupole
$\frac{19}{2}^+ \rightarrow \frac{15}{2}^+$	1101.3(1)	1.12(7)	1.1(2)	1.0(2)	Quadrupole
$\frac{35}{2}^+ \rightarrow \frac{31}{2}^+$	1104.0(1)	0.70(4)	1.3(3)	1.1(3)	Quadrupole
$\frac{39}{2}^- \rightarrow \frac{35}{2}^-$	1127.9(1)	4.6(2)	1.26(5)	1.03(4)	Quadrupole
$\frac{23}{2}^- \rightarrow \frac{19}{2}^-$	1160.4(1)	2.8(2)	1.18(9)	1.2(1)	Quadrupole
$\frac{29}{2}^+ \rightarrow \frac{25}{2}^+$	1180.9(1)	0.87(5)	1.1(2)	1.1(3)	Quadrupole
$\frac{33}{2}^+ \rightarrow \frac{29}{2}^+$	1204.4(1)	3.3(2)	1.16(8)	1.37(9)	Quadrupole
$\frac{27}{2}^- \rightarrow \frac{23}{2}^-$	1205.4(1)	0.61(5)	1.2(2)	1.0(2)	Quadrupole
$\frac{31}{2}^- \rightarrow \frac{27}{2}^-$	1338.9(2)	0.51(5)			
$\frac{35}{2}^- \rightarrow \frac{31}{2}^-$	1354.9(1)	2.6(1)	1.2(1)	1.1(1)	Quadrupole
$\frac{43}{2}^- \rightarrow \frac{39}{2}^-$	1422.9(1)	0.65(4)	1.19(7)	1.33(7)	Quadrupole
$(\frac{51}{2}^-) \rightarrow \frac{47}{2}^-$	1494(1)	0.3(3)			
$\frac{35}{2}^+ \rightarrow \frac{31}{2}^+$	1608.3(1)	0.26(3)	1.3(4)	1.5(6)	Quadrupole

[a] Mixed with a 902.5-keV transition.

[b] Mixed with a 904.5-keV transition.

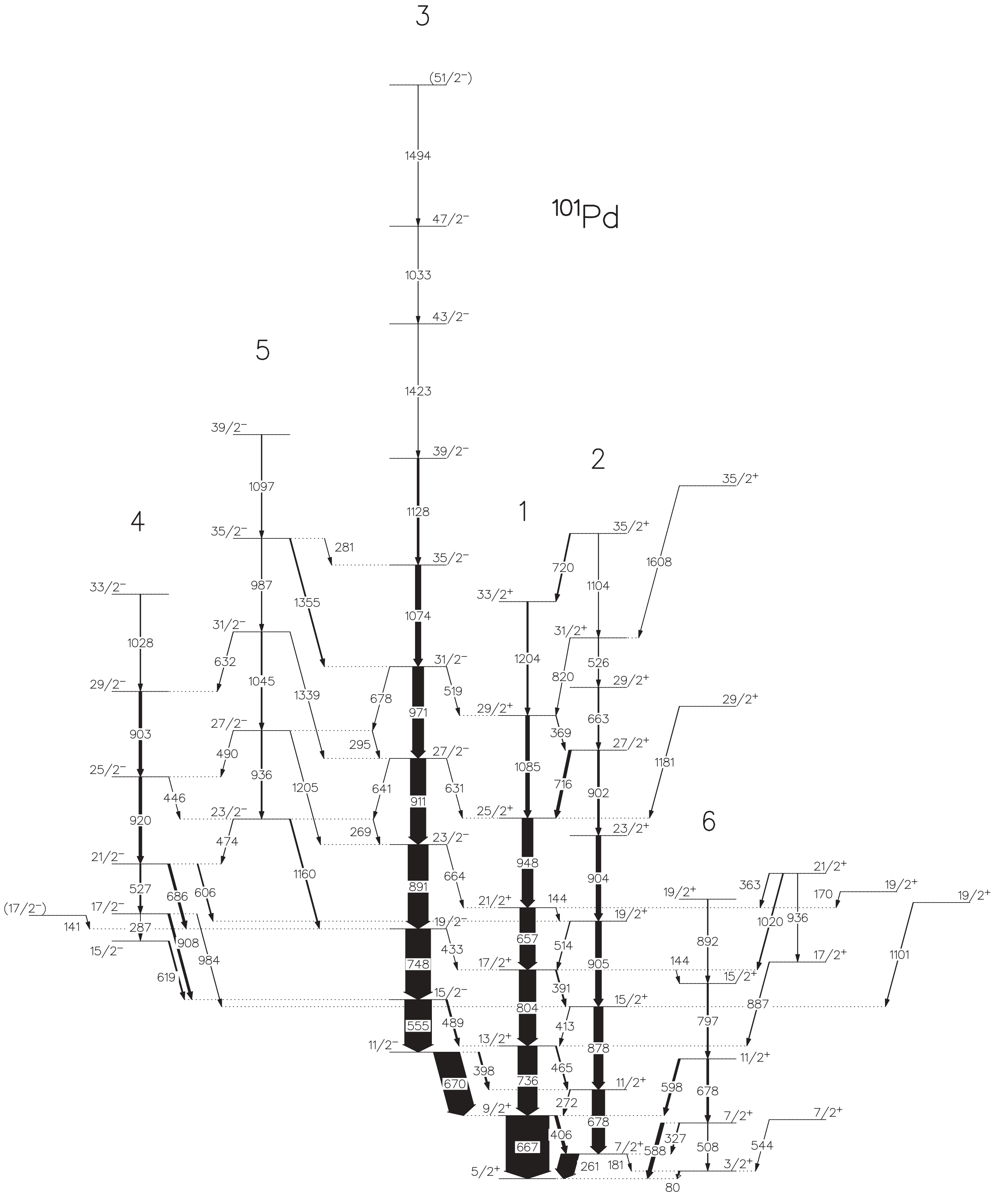

FIG. 4. Level scheme of ^{101}Pd proposed based on analysis of the $E_\gamma - E_\gamma$ matrix. The bands are labeled 1 to 6 for reference in the text.

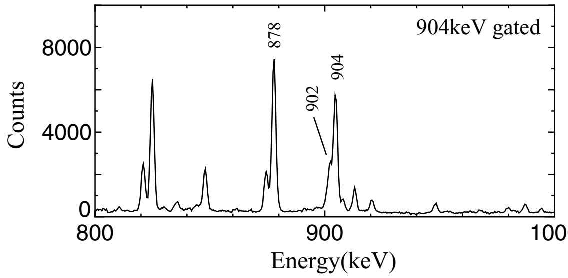

FIG. 5. An expanded plot of the spectrum obtained by setting gates on the 904-keV and 905-keV transitions in band 2.

III. DISCUSSION

As described in the previous section, we observed six bands, of which one is new and five are partially known. Due to the numerous interband transitions observed, we first discuss the implications of the properties of those transitions.

A. Properties of $M1$ transitions between bands 1 and 2

The low-spin parts of bands 1 and 2 are interpreted as rotational aligned bands built on neutron $d_{5/2}$ and $g_{7/2}$ orbitals, respectively [15]. Since these are normal-parity orbitals, it is natural to expect some mixing between them. In this regard, numerous $M1$ transitions were observed between bands 1 and 2 in the present experiment, and the branching ratios for these transitions relative to in-band transitions are summarized in terms of $B(M1)/B(E2)$ ratios in Table II. As shown in the previous section, "structure 1" and "band 2" as identified by Zhou *et al.* [16] are merged into band 2 presented here, and the 1189-keV $E2$ transition reported by Zhou *et al.* is replaced by a cascade of 526- and 663-keV $M1$ transitions. Such intervening cascade $M1$ transitions seem rather unusual from the perspective of the normal band structure. However, an abrupt increase in $B(M1)/B(E2)$ is clearly seen above $\frac{23}{2}^{+}$ for band 2 in the table. Considering that the maximum spin for the configuration $(\nu g_{7/2} d_{5/2})^5$ is $\frac{23}{2}^{+}$, this increase appears to indicate contribution from proton orbitals above $\frac{23}{2}^{+}$. This contribution may be the cause for the irregular behavior in the upper part of band 2. Zhou *et al.* interpreted the properties of bands 1 and 2 within the framework of the cranked shell model [17] and suggested that alignment of $g_{9/2}$ protons can be expected.

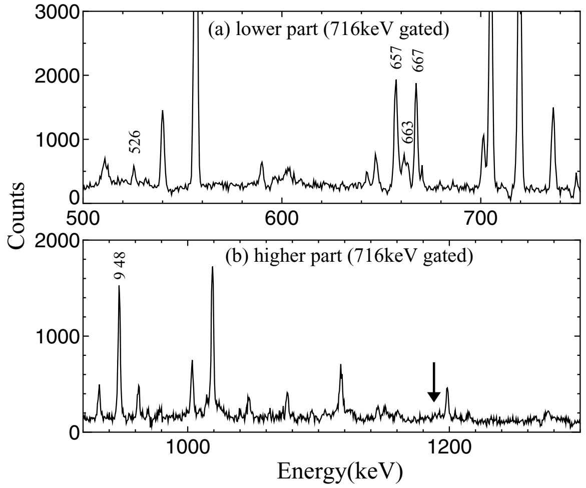

FIG. 6. A γ-γ coincidence spectrum obtained by setting a gate on the 716-keV transition from $\frac{27}{2}^{+}$ in band 2 to $\frac{25}{2}^{+}$ in band 1. Panel (a) shows the lower part, in which the 526- and 663-keV peaks are clearly seen, while panel (b) shows the higher part, in which there is no peak at the position of 1189 keV (indicated by an arrow).

TABLE II. $B(M1)/B(E2)$ ratios for transitions between bands 1 and 2 relative to in-band transitions. Dipole and quadrupole transitions are assumed to be pure $M1$ and pure $E2$ transitions, respectively. The upper or lower bounds are derived by taking $I_\gamma = 0.1$ in cases where either $M1$ or $E2$ has not been observed.

Initial spin I_i	$\frac{B(M1)}{B(E2)}\left(\frac{\mu_N}{eb}\right)^2$
$\frac{9}{2}^{+}$	0.092(7)
$\frac{11}{2}^{+}$	0.25(2)
$\frac{13}{2}^{+}$	0.087(6)
$\frac{15}{2}^{+}$	0.19(2)
$\frac{17}{2}^{+}$	0.28(2)
$\frac{19}{2}^{+}$	0.32(3)
$\frac{21}{2}^{+}$	0.13(1)
$\frac{23}{2}^{+}$	<0.009
$\frac{25}{2}^{+}$	<0.3
$\frac{27}{2}^{+}$	1.6(1)
$\frac{29}{2}^{+}$	2.5(2)
$\frac{31}{2}^{+}$	>10
$\frac{33}{2}^{+}$	<1
$\frac{35}{2}^{+}$	11(1)

B. Properties of band 3

Zhou *et al.* interpreted the properties of band 3 within the framework of the cranked shell model [17] and suggested

TABLE III. $B(E1)/B(E2)$ ratios for transitions from band 3 to band 1 relative to in-band transitions. Similar $E1$ transitions in ^{100}Pd are also listed for comparison.

Nuclide	Initial spin I_i	$\frac{B(E1)}{B(E2)}(10^{-6}\ \mathrm{fm}^{-2})$
^{101}Pd		
	$\frac{15}{2}^{-}$	0.021(2)
	$\frac{19}{2}^{-}$	0.013(4)
	$\frac{23}{2}^{-}$	0.008(2)
	$\frac{27}{2}^{-}$	0.014(2)
	$\frac{31}{2}^{-}$	0.102(8)
^{100}Pd		
	11^{-}	0.015(2)
	13^{-}	0.014(2)
	15^{-}	0.016(3)
	17^{-}	0.113(6)

TABLE IV. $B(E2)$ ratios for transitions from band 5 to band 3 and $B(M1)/B(E2)$ ratios for transitions from band 5 to band 4, both of which are relative to in-band transitions.

Initial spin I_i	$B(E2)$ ratios	$\frac{B(M1)}{B(E2)}\left(\frac{\mu_N}{eb}\right)^2$
$\frac{27}{2}^-$	0.067(7)	0.55(5)
$\frac{31}{2}^-$	0.059(7)	1.06(8)
$\frac{35}{2}^-$	0.38(3)	

that alignment of $g_{9/2}$ protons can be expected to occur first at a slightly lower rotational frequency than in the case of alignment of $g_{7/2}$ neutrons. Since the framework of AMR itself includes a gradual alignment of high-j protons, it would be interesting to study whether the properties of band 3 can be described by combining two subsequent AMR bands with neutron alignments.

Next, we proceed to a detailed discussion in support of our identification of band 3 as AMR. As described in the Introduction, AMR would appear as a regular band which consists of $\Delta I = 2$ cascade transitions with extremely small B(E2) values. It is clear that lifetime measurements are needed to confirm these properties. However, before that, it is important to determine whether a promising candidate exists based on information obtained from the level scheme. For that purpose, we employ a semiclassical particle-rotor model extended to include neutron alignments. First, we briefly describe the model in Sec. III B1. In the first part of Sec. III B2, the predictions of the model are compared with experimental data for cases confirmed as AMR in Cd isotopes to examine the applicability of the model. Lastly, we address the question of whether band 3 is a possible candidate for AMR by comparing the predictions of the model with experimental data for ^{100,101}Pd.

1. Semiclassical particle-rotor model including neutron alignments

The semiclassical particle-rotor model (SCM) was devised by Macchiavelli *et al.* to study the competition between the shears mechanism and the rotation of the core [1,21]. In SCM, high-j protons and high-j neutron holes are represented by classical angular momentum vectors (blades), and the total energy is expressed as the sum of the rotational energy of the core and effective interactions of the form $V_2P_2(\theta)$ between blades. This model was originally extended by us to include both MR and AMR on the condition that the magnitudes of all proton and neutron blades were the same [22]. This restriction was recently lifted by Choudhury *et al.* in an attempt to interpret higher-spin states of the negative-parity yrast band in ^{105}Cd as AMR [7], where the configuration of $(\pi g_{9/2}^{-2}) \otimes \nu[h_{11/2}(g_{7/2})^2]$ was considered. Since it is worth exploring the possibility that the entire negative-parity yrast band in ^{105}Cd can be described as AMR, in this study we extended the semiclassical model to include neutron alignments. Figure 7 illustrates how the total angular momentum $\vec{I}$ is generated from the proton-hole blades $\vec{J}_{\pi1}$, $\vec{J}_{\pi2}$, the neutron blade $\vec{J}_\nu$, and the rotation $\vec{R}$ of the core. Here, we assume that $\vec{J}_{\pi1}$ and $\vec{J}_{\pi2}$ consist of n_π proton holes with mutually aligned angular momenta, and $\vec{J}_\nu$ consists of n_ν neutrons with rotation-aligned angular momenta. The dynamic variable is θ, which is the angle between the proton-hole blade and the neutron blade. In this case, the total energy is the sum of the rotational energy of the core and effective interactions of the form $V_2P_2(\theta)$ between blades. The sign of V_2 is negative for particle-particle interactions and positive for particle-hole interactions. The magnitude of V_2 depends on the number of particle-particle or particle-hole pairs. The magnitude of the effective interaction for a pair is assumed to be equal to V_0 for both particle-particle and particle-hole combinations. Consequently, the energy formula is given as follows by setting $\hbar = 1$

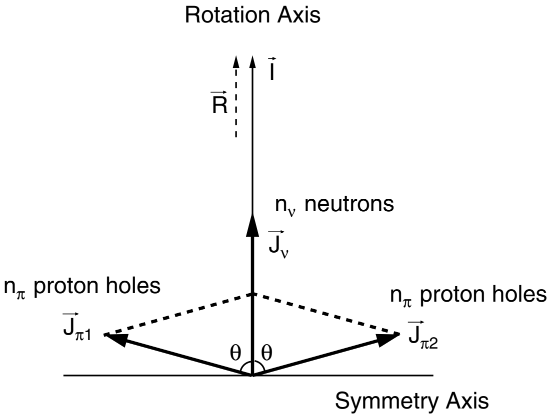

FIG. 7. Schematic representation of the angular momentum coupling of the proton-hole blades ($\vec{J}_{\pi1}$ and $\vec{J}_{\pi2}$), the neutron blade ($\vec{J}_\nu$), and the rotation ($\vec{R}$) of the core. The angular momenta $\vec{J}_{\pi1}$ and $\vec{J}_{\pi2}$ are the sum of the individual angular momenta of n_π proton holes aligned to each other. The angular momentum $\vec{J}_\nu$ is the sum of individual angular momenta of n_ν neutrons aligned to the rotational axis, and the angular momentum $\vec{R}$ is assumed to be parallel to the total angular momentum $\vec{I}$.

$$E(I,\theta) = \frac{(\vec{I} - \vec{J}_{\pi1} - \vec{J}_{\pi2} - \vec{J}_\nu)^2}{2\mathrm{Im}} + 2V_0 n_\pi n_\nu \times \left(\frac{3\cos^2\theta - 1}{2}\right) - V_0 n_\pi^2 \left(\frac{3\cos^2 2\theta - 3}{2}\right) + I\omega_0,$$

where the nomenclature introduced in Fig. 7 is used for the angular momentum vectors and Im stands for the moment of inertia of the core. The functional form $P_2(\theta) - 1$ is used as the effective interaction for the particle-particle combination to ensure that the interaction can be 0 at $\theta = 0$. The last term is introduced to reproduce the excitation energy of the bandhead, although its form is justified only *a posteriori*. We assume $J_{\pi1} = J_{\pi2} = J_\pi$ in the following calculation. By setting $(\frac{\partial E}{\partial \theta})_I = 0$, the value of θ that minimizes $E(I,\theta)$ is obtained for any given value of I as follows:

$$I = (2J_\pi \cos\theta + J_\nu) + \frac{3\mathrm{Im}V_0}{J_\pi}\cos\theta\left(n_\pi n_\nu - 2n_\pi^2\cos 2\theta\right).$$

Then, ω is expressed from the canonical relation $\omega = \frac{\partial E}{\partial I}$ as follows:

$$\omega = \omega_0 + \frac{3V_0}{J_\pi}\cos\theta\left(n_\pi n_\nu - 2n_\pi^2\cos 2\theta\right).$$

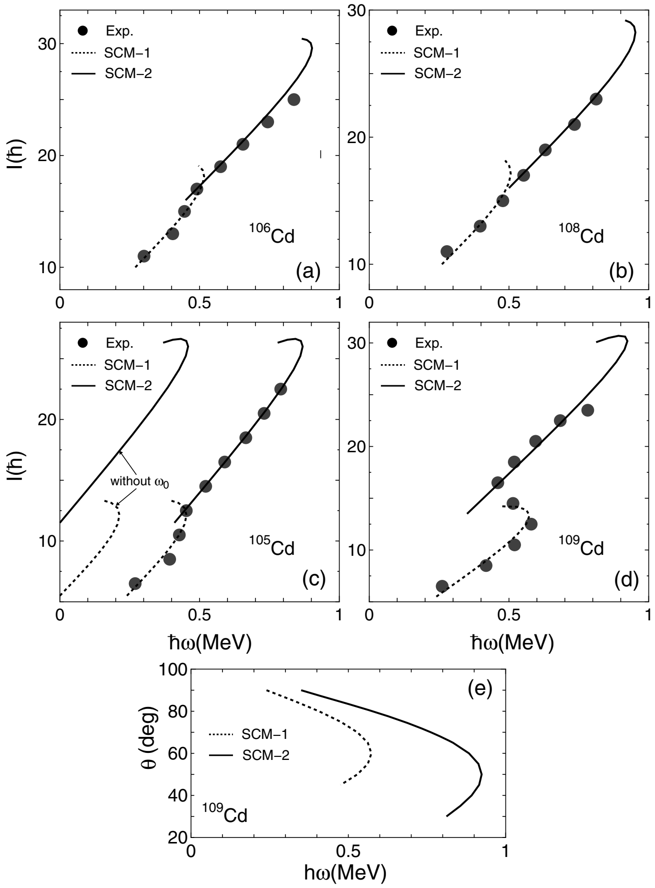

FIG. 8. I-ω plots of experimental results for Cd isotopes are compared with corresponding plots of results obtained with the semiclassical model in (a) ^{106}Cd [8], (b) ^{108}Cd [8], (c) ^{105}Cd [7], and (d) ^{109}Cd [11]. The variation in θ along the band is shown in (e) for the case of ^{109}Cd. The parameters used for the calculation are described in the text, and a plot of the calculation results without ω_0 is also shown in (c) ^{105}Cd for reference.

2. *Comparison of I-ω plots of calculation and experimental results*

The I-ω plots of results obtained from calculations using the semiclassical model described above can be compared with the corresponding plots of known examples of Cd isotopes studied experimentally, as shown in Fig. 8. Since Cd isotopes include two proton holes in the $Z = 50$ shell, $\pi g_{9/2}^{-2}$ is taken as the proton configuration. Rotational alignments of $\nu g_{7/2}^2$ or $\nu h_{11/2}^2$ are included while we consider the neutron configuration to describe the entire band. Specific configurations and parameters used in the SCM calculation are shown in the Table V, where Im, V_0, and ω_0 are regarded as free parameters to be fitted for each band.

Excellent agreement is obtained for the entire negative-parity yrast band in ^{105}Cd, as seen in Fig. 8(c). Therefore, we proceed to compare I-ω plots for the AMR of neighboring Cd isotopes, which have already been established from lifetime measurements, with the SCM calculation results in the other panels of Fig. 8. It is found that equally close agreement can be achieved within a reasonable range of parameters for the cases considered here, despite the fact that Im, V_0, and ω_0 are regarded as free parameters. The experimental curves exhibit a linear I-ω dependence, with the exception of a "kink" in the curve between the lower and upper parts of the band. A simple collective rotor with a constant moment of inertia would also describe a linear I-ω dependence, however, one merit of our model is its ability to describe the alignment process as well. To clarify this point, the variation in θ along the band is shown in Fig. 8(e) for the case of ^{109}Cd. The contribution from both the shears and the collective rotation increase smoothly until proton blades are approximately half-closed. At that stage, the contribution of rotation starts to decrease while the blades continue to close, after which the proton blades reopen in exchange of the neutron alignments, and the new AMR band starts again.

Encouraged by this result, we describe band 3 of ^{101}Pd observed in this experiment and the tentatively claimed AMR of ^{100}Pd [10] by using the semiclassical model with neutron alignments. Since Pd isotopes include four proton holes in the $Z = 50$ shell, here we consider $\pi g_{9/2}^{-4}$ as the proton configuration. I-ω plots of experimental results are compared with plots of SCM calculation results in Fig. 9. The configurations and parameters used in the SCM calculations are listed in Table VI. Clearly, the entire bands can be described reasonably well in a consistent way by the SCM calculation, although the experimental data are often scattered. Therefore, it is reasonable to conclude that band 3 in ^{101}Pd might be a suitable candidate for AMR.

TABLE V. Configuration and parameters used for Cd isotopes in the semiclassical particle-rotor model (SCM) calculation, which is classified into type 1 or 2 depending on the absence or presence of two-neutron alignment. Im, V_0, and ω_0 are taken as free parameters to be fitted for each band.

Nuclide(type)	Configuration	$J_\pi(n_\pi)$	$J_\nu(n_\nu)$	Im(1/MeV)	V_0(MeV)	ω_0(MeV)
^{105}Cd(SCM-1)	$(\pi g_{9/2}^{-2}) \otimes (\nu h_{11/2})$	9/2(1)	11/2(1)	10	0.32	0.24
^{105}Cd(SCM-2)	$(\pi g_{9/2}^{-2}) \otimes (\nu h_{11/2} g_{7/2}^2)$	9/2(1)	23/2(3)	19	0.32	0.41
^{106}Cd(SCM-1)	$(\pi g_{9/2}^{-2}) \otimes (\nu h_{11/2}^2)$	9/2(1)	10(2)	12	0.24	0.27
^{106}Cd(SCM-2)	$(\pi g_{9/2}^{-2}) \otimes (\nu h_{11/2}^2 g_{7/2}^2)$	9/2(1)	16(4)	16	0.24	0.45
^{108}Cd(SCM-1)	$(\pi g_{9/2}^{-2}) \otimes (\nu h_{11/2}^2)$	9/2(1)	10(2)	8	0.24	0.26
^{108}Cd(SCM-2)	$(\pi g_{9/2}^{-2}) \otimes (\nu h_{11/2}^2 g_{7/2}^2)$	9/2(1)	16(4)	13	0.24	0.50
^{109}Cd(SCM-1)	$(\pi g_{9/2}^{-2}) \otimes (\nu h_{11/2})$	9/2(1)	11/2(1)	10	0.50	0.24
^{109}Cd(SCM-2)	$(\pi g_{9/2}^{-2}) \otimes (\nu h_{11/2}^3)$	9/2(1)	27/2(3)	19	0.40	0.35

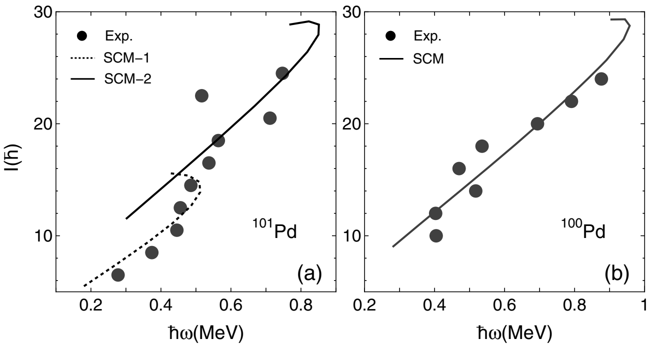

FIG. 9. I-ω plots of the results for Pd isotopes obtained in the experiment are compared with corresponding plots of results obtained with the semiclassical model in (a) ^{101}Pd and (b) ^{100}Pd [10]. The parameters used for the calculation are described in the text.

C. Properties of $E1$ transitions from band 3 to band 1

The low-spin part of band 3 has been interpreted as a rotational aligned band built on the neutron $h_{11/2}$ orbital [15]. Several $E1$ transitions have been observed from these states to the members of band 1, and the branching ratios relative to the in-band transitions are summarized in terms of $B(E1)/B(E2)$ ratios in Table III. The conventional interpretation is that the observation of enhanced $\Delta I = 1$ $E1$ transitions indicates the presence of octupole collectivity, and that could also be the case for band 3. In general, octupole correlations can be expected in the cases where the Fermi surface of protons or neutrons lies between orbitals whose orbital and total angular momenta differ by three units (i.e., $\Delta l = \Delta j = 3$). In this regard, $\nu d_{5/2}$ and $\nu h_{11/2}$ are such orbitals in the region which we are currently exploring. In fact, similar $E1$ transitions have been observed, and their enhancement has been discussed for a neighboring isotope ^{100}Pd [4]. To illustrate the enhancement in ^{101}Pd, $B(E1)/B(E2)$ ratios in ^{100}Pd are also listed in Table III for comparison. It is clear that there is close similarity between the magnitudes in ^{100}Pd and those in ^{101}Pd. An increase by an order of magnitude is seen in both nuclei at certain spins, namely at $\frac{31}{2}^-$ in ^{101}Pd and 17^- in ^{100}Pd. An increased ratio can mean that $B(E1)$ has increased, that $B(E2)$ has decreased, or possibly both. If band 3 is an AMR band, the $B(E2)$ values are expected to decrease at higher spins in the band. Thus, the currently available information is insufficient to conclude whether the $B(E1)$ values increase and octupole collectivity develops at higher spins. The clarification of this point is left for future measurements of lifetimes in this band to determine the absolute decay strengths.

D. Properties of bands 4 and 5

According to the interpretation provided by Zhou *et al.*, band 4 might be a signature partner of band 3 based on their similar transition energies [17]. Band 5 was newly observed in the present experiment, whereby it was found to decay via stretched $M1$ transitions to band 4. Consequently, since the signature of band 5 is different from that of band 4, it is more probable for band 5 to be a signature partner of band 4. The level spacings in Fig. 4 show a band crossing at $\hbar\omega = 0.45$ and 0.49 MeV for bands 4 and 5, respectively. These values are close to the theoretical prediction of 0.48 MeV for the alignment of $g_{9/2}$ protons obtained by the cranked shell model [17]. Furthermore, the $B(M1)/B(E2)$ ratios for $M1$ transitions from band 5 to band 4 are summarized in Table IV, where it should be noted that there is a change before and after the band crossing. Specifically, while $M1$ transitions with $B(M1)/B(E2) \sim 1$ have been observed before, no $M1$ transitions have been observed after the crossing. This appears to be consistent with the alignment of high-j protons. Therefore, bands 4 and 5 may be interpreted as signature partners of $\frac{1}{2}^-$[550]. The observation of both signatures of the $\frac{1}{2}^-$[550] band provides indirect support of the interpretation of band 3 as AMR.

Since bands 5 and 3 have the same signature and similar excitation energies, band mixing can be naturally expected in this case. Band 5 decays to band 3 via $E2$ transitions, whose $B(E2)$ ratios are summarized in Table IV. The fact that interband transitions are comparable in strength to in-band transitions at $\frac{35}{2}^-$ indicates that the effects of band mixing may become substantial around this spin region.

IV. SUMMARY

We presented the results of a study on the high-spin states of ^{101}Pd, which were obtained through in-beam γ-ray spectroscopy using the reaction ^{68}Zn(^{37}Cl, $1p3n$). Two of the known bands were revised or extended to higher-spin states, and a new band was observed. Moreover, a number of newly observed interband transitions appear to confirm the band structures. Regarding the observation of $E1$ transitions between the $\nu h_{11/2}$ band and the $\nu d_{5/2}$ band, the currently available information is insufficient to conclusively claim the existence of octupole collectivity.

We also extended the semiclassical particle-rotor model for AMR to include neutron alignments, whereby we found that our schematic model can describe the I-ω plots for known cases of Cd isotopes as well as for tentatively claimed cases of ^{100,101}Pd in a consistent way.

TABLE VI. Configuration and parameters used for ^{100,101}Pd in the SCM calculation, which is classified into type 1 or 2 depending on the absence or presence of two-neutron alignment. Im, V_0, and ω_0 are taken as free parameters to be fitted for each band.

Nuclide(type)	Configuration	$J_\pi(n_\pi)$	$J_\nu(n_\nu)$	Im(1/MeV)	V_0(MeV)	ω_0(MeV)
^{100}Pd(SCM)	$(\pi g_{9/2}^{-4}) \otimes [\nu h_{11/2}(g_{7/2}d_{5/2})^3]$	6(2)	9(4)	19	0.22	0.28
^{101}Pd(SCM-1)	$(\pi g_{9/2}^{-4}) \otimes (\nu h_{11/2})$	6(2)	11/2(1)	10	0.22	0.18
^{101}Pd(SCM-2)	$(\pi g_{9/2}^{-4}) \otimes (\nu h_{11/2} g_{7/2}^2)$	6(2)	23/2(3)	19	0.22	0.30

Lifetime measurements by Doppler shift attenuation methods are desirable to confirm the AMR character of band 3 in ^{101}Pd.

ACKNOWLEDGMENTS

We thank the team operating the JAEA tandem accelerator for providing the heavy-ion beams used in the experiment.

[1] R. M. Clark and A. O. Macchiavelli, Annu. Rev. Nucl. Part. Sci. **50**, 1 (2000).
[2] S. Frauendorf, Rev. Mod. Phys. **73**, 463 (2001).
[3] A. J. Simons, R. Wadsworth, D. G. Jenkins, R. M. Clark, M. Cromaz, M. A. Deleplanque, R. M. Diamond, P. Fallon, G. J. Lane, I. Y. Lee *et al.*, Phys. Rev. Lett. **91**, 162501 (2003).
[4] G. E. Perez, D. Sohler, A. Algora, Z. Dombrádi, B. M. Nyakó, J. Timár, L. Zolnai, R. Wyss, J. Cederkäll, A. Johnson *et al.*, Nucl. Phys. A **686**, 41 (2001).
[5] J. Gizon, B. M. Nyakó, J. Timár, A. Gizon, L. Zolnai, A. J. Boston, G. Căta-Danil, J. Genevey, D. T. Joss, N. J. O'Brien *et al.*, Phys. Lett. B **410**, 95 (1997).
[6] D. Sohler, J. Timár, Z. Dombrádi, J. Cederkäll, J. Huijnen, M. Lipoglavšek, M. Palacz, A. Atac, C. Fahlander, H. Grawe *et al.*, Nucl. Phys. A **733**, 37 (2004).
[7] D. Choudhury, A. K. Jain, M. Patial, N. Gupta, P. Arumugam, A. Dhal, R. K. Sinha, L. Chaturvedi, P. K. Joshi, T. Trivedi *et al.*, Phys. Rev. C **82**, 061308(R) (2010).
[8] A. J. Simons, R. Wadsworth, D. G. Jenkins, R. M. Clark, M. Cromaz, M. A. Deleplanque, R. M. Diamond, P. Fallon, G. J. Lane, I. Y. Lee *et al.*, Phys. Rev. C **72**, 024318 (2005).
[9] P. Datta, S. Chattopadhyay, S. Bhattacharya, T. K. Ghosh, A. Goswami, S. Pal, M. S. Sarkar, H. C. Jain, P. K. Joshi, R. K. Bhowmik *et al.*, Phys. Rev. C **71**, 041305(R) (2005).
[10] S. Zhu, U. Garg, A. V. Afanasjev, S. Frauendorf, B. Kharraja, S. S. Ghugre, S. N. Chintalapudi, R. V. F. Janssens, M. P. Carpenter, F. G. Kondev *et al.*, Phys. Rev. C **64**, 041302(R) (2001).
[11] C. J. Chiara, S. J. Asztalos, B. Busse, R. M. Clark, M. Cromaz, M. A. Deleplanque, R. M. Diamond, P. Fallon, D. B. Fossan, D. G. Jenkins *et al.*, Phys. Rev. C **61**, 034318 (2000).
[12] D. R. Doty, P. Charoenkwan, J. W. Sunier, and J. R. Richardson, Nucl. Phys. A **103**, 404 (1967).
[13] S. I. Hayakawa, I. R. Hyman, and J. K. P. Lee, Nucl. Phys. A **296**, 251 (1978).
[14] P. C. Simms, G. J. Smith, F. A. Rickey, J. A. Grau, J. R. Tesmer, and R. M. Steffen, Phys. Rev. C **9**, 684 (1974).
[15] R. Popli, F. A. Rickey, and P. C. Simms, Phys. Rev. C **22**, 1121 (1980).
[16] H. B. Zhou, X. H. Zhou, Y. H. Zhang, M. Oshima, Y. Toh, M. Koizumi, A. Osa, and Y. Hatsukawa, Chin. Phys. C **34**, 1598 (2010).
[17] H. B. Zhou, X. H. Zhou, Y. H. Zhang, Y. Zheng, M. L. Liu, N. T. Zhang, L. Chen, S. T. Wang, G. S. Li, H. X. Wang *et al.*, Eur. Phys. J. A **47**, 107 (2011).
[18] K. Furuno, M. Oshima, T. Komatsubara, K. Furutaka, T. Hayakawa, M. Kidera, Y. Hatsukawa, M. Matsuda, S. Mitarai, T. Shizuma *et al.*, Nucl. Instrum. Methods Phys. Res. A **421**, 211 (1999).
[19] D. C. Radford, Nucl. Instrum. Methods Phys. Res. A **361**, 297 (1995).
[20] M. Piiparinen, A. Ataç, J. Blomqvist, G. B. Hagemann, B. Herskind, R. Julin, S. Juutinen, A. Lampinen, J. Nyberg, G. Sletten *et al.*, Nucl. Phys. A **605**, 191 (1996).
[21] A. O. Macchiavelli, R. M. Clark, M. A. Deleplanque, R. M. Diamond, P. Fallon, I. Y. Lee, F. S. Stephens, and K. Vetter, Phys. Lett. B **450**, 1 (1999).
[22] M. Sugawara, Y. Toh, M. Oshima, M. Koizumi, A. Osa, A. Kimura, Y. Hatsukawa, J. Goto, H. Kusakari, T. Morikawa *et al.*, Phys. Rev. C **79**, 064321 (2009).